Evolution of the proton ring current energy distribution during 21–25 April 2001 storm

N. Y. Ganushkina,[1] T. I. Pulkkinen,[1,2] A. Milillo,[3] and M. Liemohn[4]

Received 11 January 2006; revised 13 July 2006; accepted 14 August 2006; published 11 October 2006.

[1] Three ring current models are used to follow the evolution of the proton ring current during the 2001-04-21–25 storm: The ring current model combined with tracing particles numerically in the drift approximation by Ganushkina et al. (2005), the empirical model of proton fluxes in the inner magnetosphere developed by Milillo et al. (2003), and the kinetic ring current-atmosphere interaction model (RAM) by Liemohn et al. (2001). The paper focuses on the effects of the electric and magnetic field models and initial particle distributions on the final energy distribution. We examine a variety of large-scale magnetic field and convection electric field models as well as substorm-associated, smaller-scale, and time-varying electric fields. We find that (1) using more realistic magnetic field models leads to reduction of the ring current energy content by ~30%; (2) details of the global convection field have little influence on the overall ring current evolution; (3) smaller-scale impulsive electric field have profound effects on the ring current evolution, particularly with regard to the acceleration of the higher-energy particles; and (4) in the ring current models, the choice of the initial and boundary conditions have significant effects on the modeled ring current intensity and energy spectrum.

Citation: Ganushkina, N. Y., T. I. Pulkkinen, A. Milillo, and M. W. Liemohn (2006), Evolution of the proton ring current energy distribution during 21–25 April 2001 storm, *J. Geophys. Res.*, *111*, A11S08, doi:10.1029/2006JA011609.

1. Introduction

[2] The main portion of the Earth's ring current energy is carried by magnetically trapped energetic ions in the energy range of 10–200 keV. During magnetic storms, both the energy spectrum and the flux of the energetic particles undergo strong variations, and the currents these particles carry have a strong influence on the magnetic field configuration in the inner magnetosphere. Statistical results show that during the storm main phase most of the energy density is in the energy range around 30–80 keV, which changes during the recovery phase so that the energy density is concentrated at the high-energy end above 80 keV [*Ganushkina et al.*, 2005]. How, where, and when the ions are accelerated and transported to the inner magnetosphere and what processes contribute to their losses are key questions that need to be answered for better understanding of the inner magnetosphere dynamics.

[3] At present, there are several ring current models that have very different approaches to modeling the inner magnetosphere processes and that can use a variety of empirical parameterizations of the electromagnetic fields, initial and boundary conditions. The purpose of this paper is to discuss three of these models, the ring current model by *Ganushkina et al.* [2005], the empirical model of proton fluxes by *Milillo et al.* [2003], and the kinetic ring current-atmosphere interaction model (RAM) by *Liemohn et al.* [2001] and compare and contrast the model results with each other and with available observations. As an illustrative example, we analyze the storm on 2001-04-21–25, which has been selected for analysis by the Inner Magnetosphere/Storms (IM/S) Assessment Challenge (IMSAC) of the National Science Foundation Geospace Environment modeling (GEM) program.

[4] Several simulations of the ring current dynamics during storms have been successfully performed earlier [*Lee et al.*, 1983; *Takahashi et al.*, 1990; *Kozyra et al.*, 1998; *Ebihara and Ejiri*, 2000; *Jordanova et al.*, 2001a; *Liemohn et al.*, 2001]. Most of these models solve the temporal evolution of the phase space density of the ring current particles using the Boltzmann equation. In general, they include representation of the source distribution, transport equations, and loss processes (see review by *Ebihara and Ejiri* [2003]). In all approaches, models for the magnetic and electric fields are used to define particle motion in the magnetosphere. Most models use a dipole magnetic field and the electric field is taken to be either the large-scale magnetospheric convection field [*Volland*, 1973; *Stern*, 1975; *McIlwain*, 1986] or the polar cap potential mapped to the magnetosphere along equipotential magnetic field lines [*Boyle et al.*, 1997; *Weimer*, 2001].

[1] Finnish Meteorological Institute, Space Research Division, Helsinki, Finland.
[2] Also at Space Science and Applications, Los Alamos National Laboratory, Los Alamos, New Mexico, USA.
[3] Istituto di Fisica dello Spazio Interplanetario, Rome, Italy.
[4] Space Physics Research Laboratory, University of Michigan, Ann Arbor, Michigan, USA.

0148-0227/06/2006JA011609

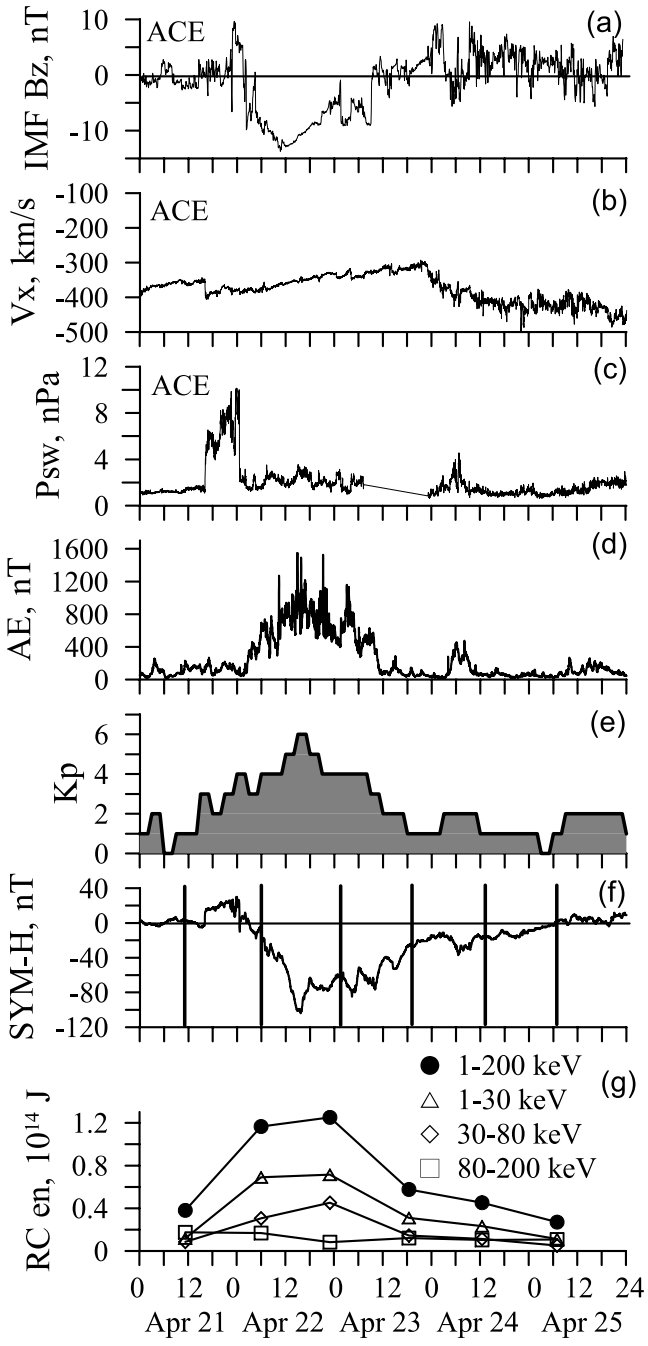

Figure 1. Overview of 21–25 April 2001 storm: (a) IMF B_z, (b) solar wind V_x, and (c) solar wind dynamic pressure as measured by the ACE spacecraft. Ground-based activity indices (d) AE, (e) Kp, (f) SYM-H, and (g) Polar CAMMICE/MICS measurements of ring current energy.

[5] The best descriptions of the terrestrial magnetic field model are given by empirical models. Statistical models such as those developed by *Tsyganenko* [1989, 2002a, 2002b] describe the magnetic field based on analytical modeling of magnetospheric current systems and fitting the model parameters to a large data set of high-altitude magnetic field measurements. While these models can give quite an accurate picture of average conditions, under extreme conditions or during dynamic events the field may deviate quite substantially from the statistical average. To overcome that problem, *Ganushkina et al.* [2004] developed a method that allows for fitting the parameters to match the conditions during individual events. They demonstrate that this can lead to a much improved fit especially during large storms that are not well represented in the large database used to create the statistical models.

[6] The electric field observations are difficult to make and separation of the large-scale properties and the smaller-scale impulsive structures is less obvious than in the case of magnetic fields. First, the shielding properties of the large-scale electric field may be very different during storms than during other times; *Rowland and Wygant* [1998] suggest that the shielding is essentially removed for high Kp conditions and the electric field increases almost linearly with decreasing radial distance. Second, recent studies have shown that most of the earthward transport of plasma and magnetic flux occurs in the form of short-duration, high-speed plasma flows, which are associated with small-scale magnetic field dipolarizations and highly fluctuating electric fields [*Baumjohann et al.*, 1990; *Angelopoulos et al.*, 1992; *Sergeev et al.*, 1996]. While these bursts are found during all activity conditions, they become stronger and more numerous during periods of higher activity. Furthermore, during substorm expansion phases, large, transient electric fields appear in the plasma sheet [*Maynard et al.*, 1996; *Aggson et al.*, 1983; *Rowland and Wygant*, 1998]. The enhanced electric fields have amplitudes up to 20 mV/m and are coincident with braking of the fast flows and dipolarization of the magnetic field [see *Tu et al.*, 2000, and references therein].

[7] Several studies have concluded that concurrent action of global convection and substorm-time dipolarization with the associated electric field variations inject plasma closer to the Earth than either process would do individually [*Fok et al.*, 1999; *Ganushkina and Pulkkinen*, 2002]. A variety of models have attempted to represent these substorm-associated electromagnetic fields [*Li et al.*, 1998; *Zaharia et al.*, 2000; *Sarris et al.*, 2002]. Employing the *Li et al.* [1998] model, *Ganushkina et al.* [2000, 2001] were able to reproduce the so-called intense nose structures consisting of plasma sheet particles in the inner magnetosphere ring current region. Furthermore, *Ganushkina et al.* [2005] incorporated fluctuating fields using the *Sarris et al.* [2002] model and demonstrated that only the substorm-associated time-varying and localized electric fields produced strong enough acceleration to yield the observed fluxes of high-energy ions in the ring current. Analogously, *Khazanov et al.* [2004a, 2004b] found that rapid time variations (of the order of a few minutes) need to be included in the convection field used to drive the RAM model to produce the buildup of a high-energy (100–1000 keV) tail to the ion and electron distribution functions. Longer time cadences, especially a 3-hour update interval as one would have using the Kp index, could not produce these enhancements.

[8] A complementary approach to ring current modeling was made by *Milillo et al.* [2001], who used data from the Charge-Energy-Mass instrument (CHEM) onboard AMPTE/CCE (Active Magnetospheric Particle Tracer Explorers/Charge Composition Explorer) satellite to formulate an empirical model for the average equatorial H^+ fluxes in the inner magnetosphere. The model gives a parametrization for

the ion distributions, and time-dependent tuning of the model parameters then gives the global evolution of the proton distribution in the equatorial magnetosphere. *Orsini et al.* [2004] demonstrated that the parameter variations can be associated with convection, injection, and diffusion processes. In particular, the model empirically identified the diffusion-associated high-energy population, which increases in energy with decreasing distance from the Earth.

[9] The paper is organized as follows: Section 2 briefly introduces the event and relevant observations. Sections 3–5 review the three models that are used to examine the ring current behavior. In the following, the models will be named the "Ganushkina model" [*Ganushkina et al.*, 2005], the "Milillo model" [*Milillo et al.*, 2003], and the "Liemohn model" [*Liemohn et al.*, 2001] for simplicity. Results from the model calculations are presented and discussed in Section 6. Sections 7 and 8 end with discussion and conclusions.

2. Storm of 21–25 April 2001

[10] The magnetic storm that took place on 21–25 April 2001 was moderate, with Dst-minimum reaching −100 nT. Figure 1 shows the interplanetary magnetic field (IMF) B_z, the solar wind velocity V_x, and the solar wind dynamic pressure, as measured by the ACE spacecraft, together with ground-based activity indices AE, Kp, and SYM-H. The bottom panel shows ring current energy measurements from the Charge and Mass Magnetospheric Ion Composition Experiment (CAMMICE) Magnetospheric Ion Composition Sensor (MICS) on board the Polar spacecraft.

[11] The event started with the arrival of a shock associated with a relatively small velocity jump of below 100 km/s, but a large density pulse, which together with the solar wind speed increase caused the pressure to jump from about 2 nPa to values reaching 10 nPa. In the sheath region after the shock, the IMF B_Z fluctuated first around zero and beginning about 2145 UT on April 21 was strongly positive. The sheath region did not drive strong auroral activity, although Kp showed slightly enhanced values around 3 for the rest of the day.

[12] The cloud arrival was marked with a prompt southward turning of the IMF B_Z at about 0130 UT on 22 April. A slow rotation is seen in all IMF components. The rotation was largest in IMF B_Y and B_Z; B_X was slightly negative at the leading edge of the cloud and rotated to a few nT positive value at the trailing edge of the cloud (not shown). In the cloud proper, the solar wind speed slowly decreased from about 400 km/s to about 300 km/s, making this a rather slow magnetic cloud. The solar wind density within the cloud fluctuated around 10 cm^{-3}, which kept the pressure fluctuating around 3 nPa.

[13] As the shock arrived, the SYM-H index jumped from around zero to 20 at first and later above 30 nT. The cloud arrival started the negative trend in the SYM-H index with the strongest activity increase occurring toward the end of the main phase during 1000–1600 UT on 22 April. After that, the recovery phase was associated with several further SYM-H enhancements during the cloud passage. The auroral-latitude activity began about 0200 UT on April 22 with the first enhancement reaching about 450 nT, which was followed by several enhancements reaching 1500 nT peak intensities. The strongest activations during the magnetic cloud were coincident with the SYM-H decreases. The Kp-index reached its maximum value of 6 at the time of the minimum SYM-H on 22 April.

[14] During the storm recovery after the cloud passage (after about 2100 UT on 23 April), the auroral activity was low and Kp values fluctuated below 2. The solar wind and IMF values were nominal, and the SYM-H index returned to zero by the early hours of 25 April.

[15] The proton ring current energy content (Figure 1g) were computed using methods introduced by *Pulkkinen et al.* [2001] and *Ganushkina et al.* [2005]. The energy density per unit volume $w(L)$ of the ring current particles in the energy range from $E_{\min}$ to $E_{\max}$ between $L = 3$, and $L = 7$ is computed from

$$w(L) = 2\pi\sqrt{2mq}\int_{E_{\min}}^{E_{\max}} dE\sqrt{E}j(E,L), \quad (1)$$

where m is the particle mass, q is the particle charge state, E is the particle energy, $j(E, L)$ is the measured particle differential flux, and L is the McIlwain L-parameter. The total ring current energy W_{RC} is computed by integration over the ring current volume which we assume, for simplicity, to be $V = 10^{23}$ m^3, corresponding to a torus with circular cross section of 2.5 R_E and mean radius of 5 R_E. No pitch angle corrections were made when mapping the observed fluxes to equatorial values. The ring current energy contents were computed separately for low (1–30 keV), medium (30–80 keV), and high (80–200 keV) energy ranges; the total energy content is computed using energies from 1 to 200 keV. These energy ranges will also be examined in presenting the model results.

[16] The modeling period has been selected, because it was selected for analysis by the Inner Magnetospheric Assessment Challenge (IMSAC) of the NSF GEM program, and therefore represents a standard period for the scientific community. However, the available data has limitations for our purposes: For example, we must assume that the ring current energy content is longitudinally symmetric. Furthermore, as discussed later, the Polar spacecraft resided at relatively high latitudes during the measurements, which limited our ability to measure the total energy content, and which probably affected the spectral shapes of the observed particle populations. Thus while the data in Figure 1 is used to motivate and guide our evaluation of the different model responses, it does not represent a final benchmark.

3. Ganushkina Model

3.1. Particle Tracing Procedure

[17] In this model, protons with 90° ± 60° pitch angles are traced under the conservation of the first and second adiabatic invariants in time-dependent magnetic and electric fields [*Ganushkina et al.*, 2005]. The initial distribution is a κ function at a boundary $R = 7$ and populated in local times 1900–0500 MLT in the equatorial plane. The distribution function is given by

$$f(E) = n\left(\frac{m}{2\pi kE_0}\right)^{3/2}\frac{\Gamma(\kappa+1)}{\Gamma(\kappa-1/2)}\left(1+\frac{E}{\kappa E_0}\right)^{-(\kappa+1)} \quad (2)$$

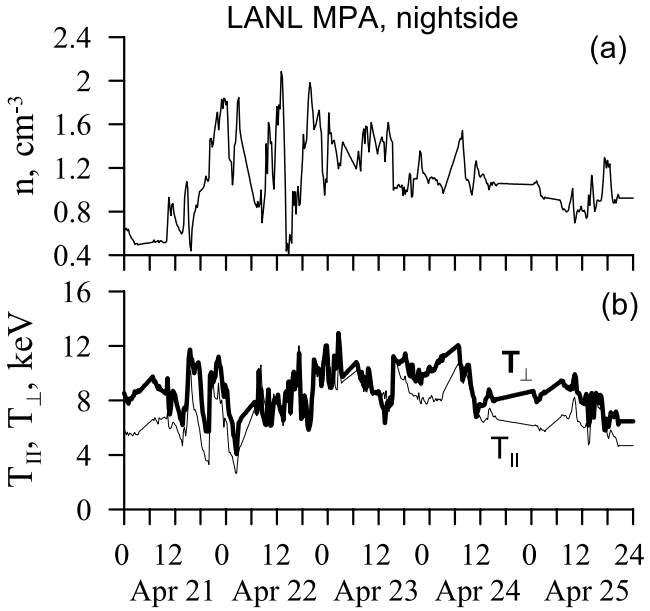

Figure 2. The 2001-04-21–25 storm: (a) number density and (b) perpendicular (thick line) and parallel (thin line) temperatures used as boundary conditions in the modeling. The values were obtained from LANL MPA instruments measuring ions in the energy range 0.1–40 keV by averaging available observations within 4 hours from local midnight from spacecraft 1991-080, 1994-084, and LANL-01A.

where n is the particle number density, m is the particle mass, $E_0 = k_B\,T\,(1 - 3/2k)$ is the particle energy at the peak of the distribution, $k_B = 1.3807\ 10^{-23}$ J/K is the Boltzmann constant, and $T = 1/3(T_{\|} + 2T_{\perp})$. The gamma functions were computed using $\kappa = 5$.

[18] The number density n and perpendicular and parallel temperature ($T_{\perp}$ and $T_{\|}$, respectively) estimates were obtained using data from the MPA instrument [*Bame et al.*, 1993] on board the Los Alamos (LANL) geostationary satellites measuring ions in the energy range 0.1–40 keV. During the period of 2001-04-21–25 data from three LANL spacecraft, 1991–080, 1994–084, and LANL-01A, were available. The number density and perpendicular and parallel temperatures were created from measurements obtained within 4 hours of local time around midnight. Values were averaged when more than one spacecraft were simultaneously in that region. When no satellites were near midnight, the data were interpolated linearly. These values were then used as time-dependent boundary conditions. Figure 2 shows time series of the number density and the perpendicular (thick line) and parallel (thin line) temperatures.

[19] The drift velocity is computed as a combination of the velocity due to the $\mathbf{E} \times \mathbf{B}$ drift and the bounce-averaged velocity due to magnetic drifts, which can be given by [*Roederer*, 1970]:

$$\langle v_0 \rangle = \frac{\mathbf{E_0} \times \mathbf{B_0}}{B_0^2} + \frac{2p}{q\tau_b B_0} \nabla I \times \mathbf{e_0}, \tag{3}$$

where

$$I = \int_{S_m}^{S_m'} \left[1 - \frac{B(s)}{B_m}\right]^{1/2} ds, \tag{4}$$

where $\mathbf{E_0}$ and $\mathbf{B_0}$ are electric and magnetic fields, respectively, in the equatorial plane, p is the particle momentum, q is the particle charge, τ_b is the bounce period, $\mathbf{e}_0$ is the unit vector in the direction of $\mathbf{B_0}$, S_m and S_m' are the particle mirror points, $B(s)$ is the magnetic field along the magnetic field line, B_m is the magnetic field at the mirror point, and ds is the element of magnetic field line length.

[20] The distribution function at the next time step is obtained assuming conservation of the distribution function along the dynamic trajectory of particles (Liouville theorem), but taking into account the losses caused by charge-exchange with $\tau_{loss} = 1/(\sigma n_0 V)$. The charge-exchange cross-section is obtained from *Janev and Smith* [1993] and the number density of neutrals n_0 from the thermospheric model MSISE 90 [*Hedin*, 1991].

3.2. Models for the Electric and Magnetic Fields

[21] The electric field models used are (1) a Volland-Stern [*Volland*, 1973; *Stern*, 1975] large-scale convection electric field model and (2) a Volland-Stern-type model where the intensity is determined by the polar cap potential obtained from *Boyle et al.* [1997]. For the magnetic field we use (1) the dipole, (2) the Tsyganenko T89 [*Tsyganenko*, 1989], and the (3) storm-time Tsyganenko T01S [*Tsyganenko*, 2002a, 2002b] magnetic field models.

[22] The Volland-Stern electric potential Φ_{conv} is given by

$$\Phi_{conv}(L, \phi) = AL^{\gamma} \sin(\phi - \phi_0), \tag{5}$$

where A determines the intensity, L is the McIlwain parameter, γ is the shielding factor, ϕ is the magnetic local time, and ϕ_0 is the offset angle from the dawn-dusk meridian. A Kp-dependent function is used for A [*Maynard and Chen*, 1975]

$$A = \frac{0.045}{(1 - 0.159Kp + 0.0093Kp^2)^3} kV/R_E^2, \tag{6}$$

where $\gamma = 2$ and $\phi_0 = 0$, with the observed Kp values.

[23] Assuming Volland-Stern-type convection and defining the intensity of the convection from the magnitude of the polar cap potential as given by *Boyle et al.* [1997] gives the potential as a function of radial distance, azimuth angle, and solar wind and IMF parameters in the form

$$\Phi_{pc}(R, \phi) = \left[1.01 \cdot 10^{-4} V_{sw}^2 + 11.1 \cdot B_{IMF} \sin^3\left(\frac{\theta_{IMF}}{2}\right)\right] \cdot \left(\frac{\sin\phi}{2}\left(\frac{R}{R_B}\right)^2\right), \tag{7}$$

where V_{sw} is the solar wind bulk speed, B_{IMF} is the magnitude of the interplanetary magnetic field, $\theta_{IMF} = \tan^{-1}(B_z/B_y)$ is the IMF clock angle, R is the radial distance from the Earth in the equatorial plane, and $R_B = 10.47R_E$. The ACE measurements of the interplanetary magnetic field and the solar wind speed were used to define the model.

Table 1. Times and Amplitudes of the Electromagnetic Pulses Launched at Substorm Onset Times Together With AE Peak Values During 2001-04-21–25

UT, hours	AE Peak, nT	E_0, mV/m
	22 April 2001	
0200	450	1.8
0435	700	2.8
0805	750	3.0
1000	1200	4.8
1200	900	3.6
1325	1000	4.0
1420	1500	6.0
1540	1200	4.8
1730	900	3.6
1945	1150	4.6
	23 April 2001	
0130	1150	4.6
0630	550	2.2
1330	200	0.8
	24 April 2001	
0430	450	1.8

[24] The observed Kp values were used to provide time variability in the T89 magnetic field model. The set of input parameters for the T01S magnetic field model includes the Dst index, solar wind dynamic pressure, IMF B_y and B_z components, and two functions G_1 and G_2 that depend on the IMF B_z and solar wind velocity that take into account the history of the solar wind. All these parameters were determined from observations.

3.3. Models for Small-Scale Electric Fields

[25] In order to further examine particle energization processes, we introduce smaller-scale, transient fields associated with the dipolarization processes in the magnetotail during the substorm onsets. The dipolarizations are modeled as earthward propagating electromagnetic pulses that are localized in radial and longitudinal directions [*Li et al.*, 1998; *Sarris et al.*, 2002]. The electric field is given as a time-dependent Gaussian pulse with a purely azimuthal electric field component that decreases away from midnight. The earthward propagation speed decreases as the pulse moves inward to mimic breaking of the flows [*Shiokawa et al.*, 1997]. In a spherical coordinate system the electric field is given by

$$\mathbf{E}_\phi = -\hat{e}_\phi E_0/E_{\max}(1 + c_1\cos(\phi - \phi_0))^p \exp\left(-\xi^2\right), \qquad (8)$$

where $\xi = [r - r_i + v(r)(t - t_a)]/d$ determines the location of the maximum intensity of the pulse, $v(r) = a + br$ is the pulse front velocity as a function of radial distance r, d is the width of the pulse, c_1 (>0) and p (>0) describe the local time dependence of the electric field amplitude, which is largest at ϕ_0, $t_a = (c_2/v_a)(1 - \cos(\phi - \phi_0))$ represents the delay of the pulse from ϕ_0 to other local times, c_2 determines the magnitude of the delay, v_a is the longitudinal speed of the pulse (assumed constant), and r_i is a parameter in the simulation that determines the arrival time of the pulse. We introduce a normalization coefficient $E_{\max}$ for the electric pulse amplitude. The normalization is needed because using equation (1) from *Sarris et al.* [2002] gives unrealistic values in excess of 1000 mV/m for the maximum $E_{\text{NewRoman(TrueType)}\}\phi}$ at midnight geosynchronous orbit. Following *Sarris et al.* [2002], we use $\phi_0 = 0$, $c_1 = 1$, $c_2 = 0.5\ R_E$, $a = 53.15$ km/s, $b = 0.0093\ \text{s}^{-1}$, $p = 8$, $v_a = 20$ km/s, $r_i = 100\ R_E$, and $d = 4\ 10^7$ m. The magnetic field disturbance from this dipolarization process is obtained from Faraday's law ($\partial\mathbf{B}/\partial t = -\nabla \times \mathbf{E}$). The total fields are always used in the drift velocity calculations.

[26] Several pulses were launched at substorm onset times during 2001-04-21–25. Assuming a scaling $E_0 = 4$ mV/m for an AE index maximum of 1000 nT [*Sarris et al.*, 2002], the ratio of the pulse amplitudes were set similar to the ratios of the peak values in the AE index. The launch times of the pulses were determined from times of rapid rise of the AE index. Table 1 contains the launch times and magnitudes of the pulses.

[27] It is important to notice that after the pulse has entered the inner magnetosphere, a residual magnetic field continues to contribute to the total magnetic field [see *Li et al.*, 1998, Figure 1]. When a set of pulses is launched, this residual field causes unrealistic gradients in the total magnetic field and hence unrealistic particle trajectories. To overcome this problem, we have introduced a damping mechanism that switches on a decay of the disturbance magnetic field from the pulse with a damping timescale τ, here selected to be 15 min.

[28] The damping is introduced after the end of the active phase of the pulse. The end of the active phase is chosen to be the time when the pulse reaches a point where the magnetic field temporal change caused by the pulse $\partial B/\partial t$ becomes equal to the magnetic field temporal change that decreases the corresponding current intensity by a factor of e during time τ. At that point, the magnetic field from the pulse is decreased exponentially by $B(t) = B(t_0)\exp(-t/\tau)$. The physical interpretation of this procedure is that after dipolarization during the substorm expansion phase, the magnetic field lines return to more tail-like configuration during the substorm recovery phase. The results with tracing under these small-scale, pulsed electric fields are discussed in section 6.2.

3.4. Defining an Initial Distribution in the Inner Magnetosphere

[29] Unfortunately, the available observational data were not sufficient to reconstruct the prestorm initial distribution of protons in the inner magnetosphere. Therefore to study the role of the initial distribution in the modeling, proton distributions obtained from the model at the end of 25 April 2001 (Figure 4a) at the end of the storm were used as the initial population in the inner magnetosphere.

4. Milillo Model

[30] The AMPTE/CHEM data allowed *Milillo et al.* [2001] to formulate an empirical model based on the equatorial, 90° pitch angle, average H^+ fluxes at L-shells between 3.0 and 9.3 and energies between 1.5 and 316 keV for low geomagnetic activity conditions. The model gives the ion distributions as a function of L-shell, energy, and MLT. In order to examine various activity conditions, the average condition model by *Milillo et al.* [2001] has been broken into several subsets. *Milillo et al.* [2003] describe the magnetospheric distributions during quiet times, while *Orsini et al.* [2004] present distributions during disturbed periods. The

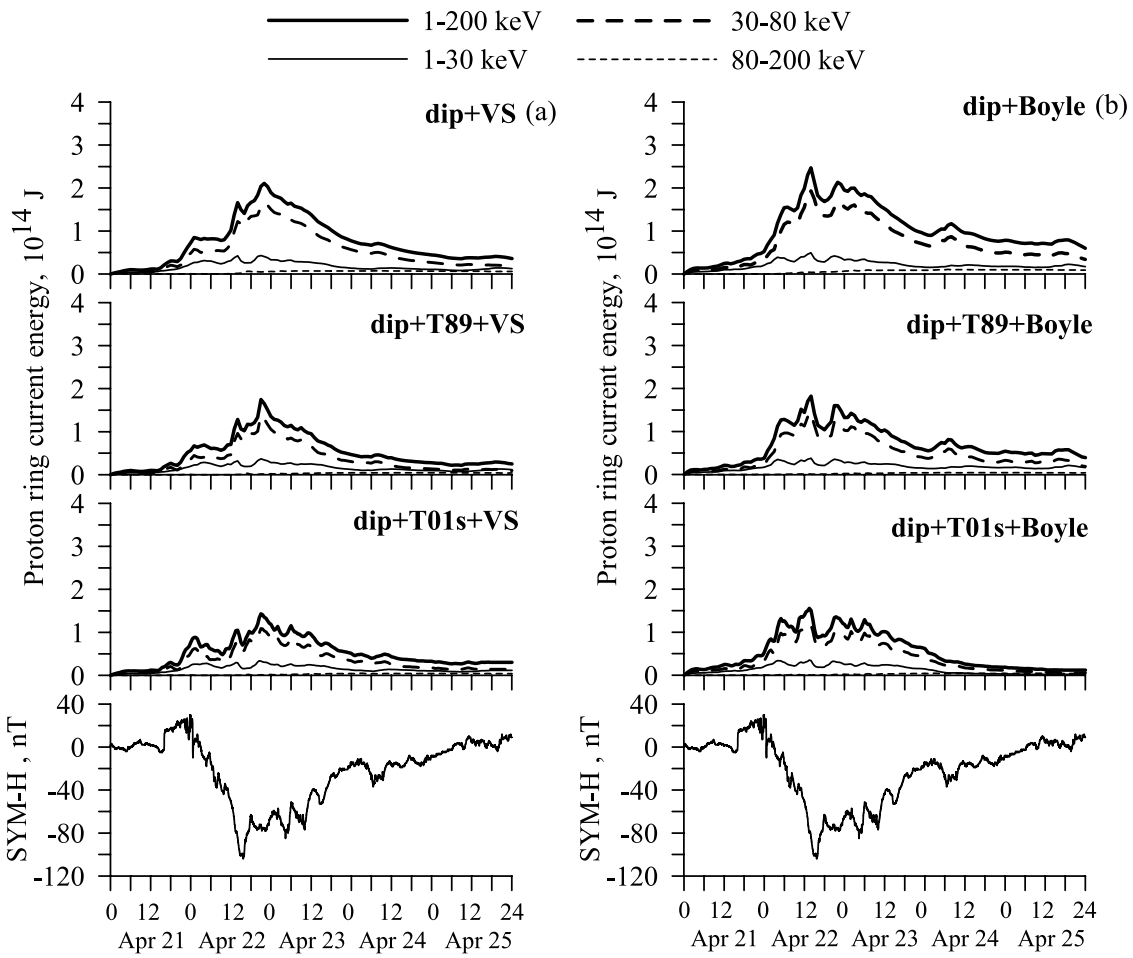

Figure 3. The 2001-04-21–25 storm, Ganushkina model, empty magnetosphere as an initial condition: proton ring current energies (in Joule) are shown for all (1–200 keV, thick solid lines), low (1–30 keV, thin solid lines), medium (30–80 keV, thick dashed lines) and high (80–200 keV, thin dashed lines) energies. (a) Left column shows tracing results using the Volland-Stern convection electric field. (b) Right column shows tracing results using the Boyle et al. polar cap potential to determine the convection strength. Rows from top to bottom show tracing results using the dipole (top row), T89 (second row), and T01S (third row) magnetic field models. The bottom row repeats the SYM-H index for reference.

functional form of the model distributions consists of two parts: (1) A Gaussian in *L*-shell added to a continuum with a Gaussian shape in energy, weighted by an *L*-shell-dependent step function describing the proton flux at intermediate energies (5–80 keV); and (2) a Gaussian in *L*-shell characterizing the high-energy population (E >40 keV). These two parts have been associated with two distinct magnetospheric populations originating from convection/injection and diffusion processes acting in the inner magnetosphere. The functional form describing the diffusion-associated higher-energy distribution must be modified to be usable with pitch angle-averaged data, as described by *Orsini et al.* [2004]. In order to obtain the time-evolving proton distributions, six model parameters were varied to fit the model to the local measurements. Applying the set of time-evolving parameters to the subset of the *Milillo et al.* [2001] model gives the global evolution of the proton distribution in the equatorial magnetosphere.

[31] *Milillo et al.* [2006] have empirically derived the H^+ distributions during the 2001-04-21–25 storm based on the *Milillo et al.* [2001] model. The pitch angle-averaged proton data measured by LANL MPA [*Bame et al.*, 1993] in the 3–45 keV energy range and SOPA [*Belian et al.*, 1992] in the 50–400 keV energy range were used to model the storm development. The time evolution of the macroscopic physical quantities, such as total energy, can then be computed from the modeled proton distributions. For these computations it was assumed that the spatial profiles of the H^+ fluxes are independent of pitch angle.

[32] For computation of the global magnetospheric distribution, *Milillo et al.* [2006] applied a set of the six time-evolving parameters to the model. The six parameters define the intensity, energy position and width of the two populations (convected/injected and diffused) present in the model. The model then gives the time-evolution of the two particle populations. Since the diffused population is generally less intense than the convected/injected population, the three parameters related to the diffused population are more difficult to determine: They have poorer statistics, and, in particular, during part of the 2001-04-21–25 storm main

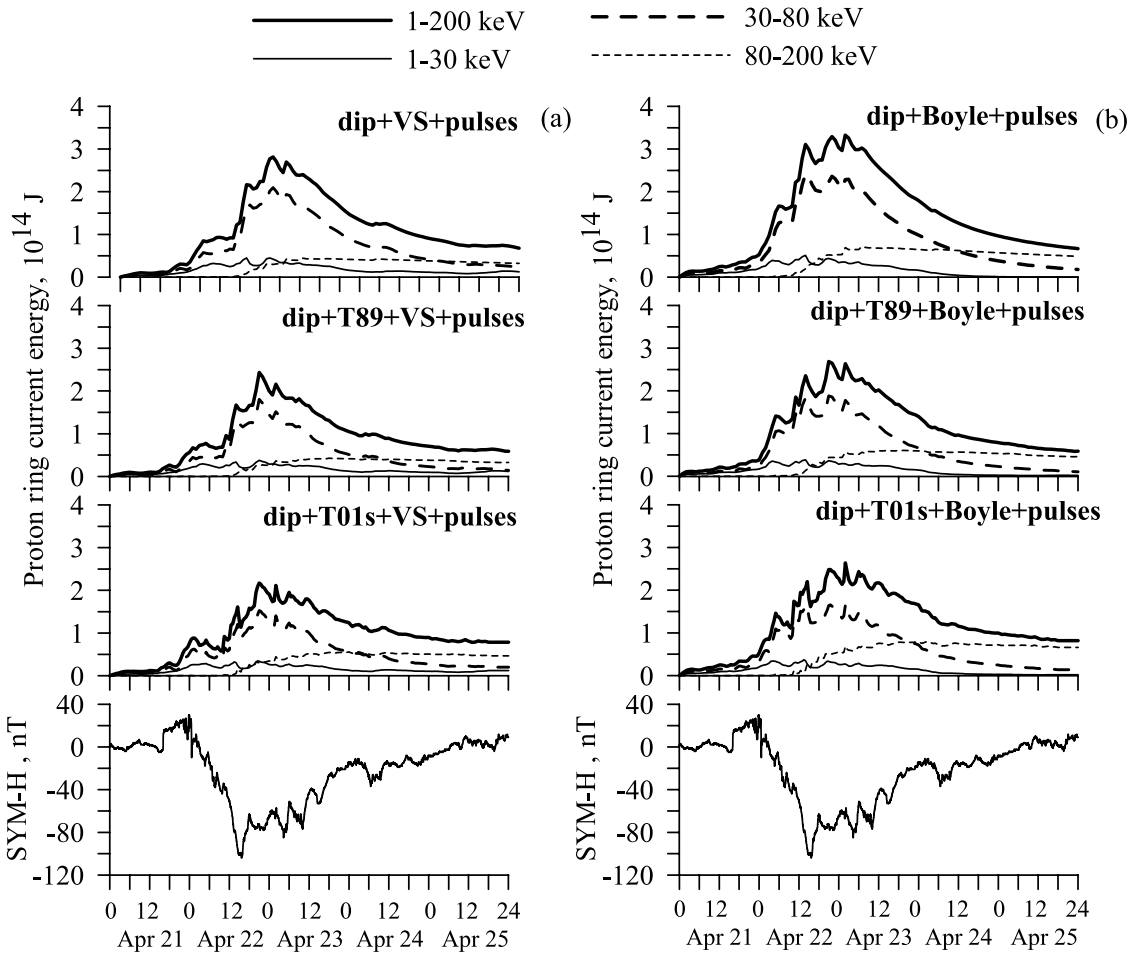

Figure 4. The 2001-04-21–25 storm, Ganushkina model, empty magnetosphere as an initial condition, electromagnetic pulses launched at substorm onset times. Format is similar to that in Figure 3.

phase, they were not determined at all [*Milillo et al.*, 2006]. During times when the parameters could not be defined, linear interpolation from one time step to the next was used.

[33] The total energy W_{RC} is computed by integrating the energy density $w(L)$ computed using equation (1) in the volume V; the results are discussed in section 6.3.

5. Liemohn Model

[34] The version of the kinetic ring current-atmosphere interaction model (RAM) used here [*Liemohn et al.*, 1999, 2001] solves the gyration- and bounce-averaged Boltzmann equation inside geostationary orbit. Using second-order accurate numerical schemes, the hot ion phase-space distribution is determined as a function of time, equatorial plane location, energy, and equatorial pitch angle, yielding a detailed description of the ring current ion population throughout near-Earth space. The initial conditions are those from *Sheldon and Hamilton* [1993] with a subsequent run for 2 days with very quiet boundary conditions scaled to roughly match the initial ring current intensity used by the other models in this study.

[35] The particle sources are specified by geostationary orbit plasma data from both LANL MPA and SOPA across the nightside outer boundary. From MPA, the number density, parallel and perpendicular temperatures were used in a bi-kappa distribution with $\kappa = 5$. The MPA number density was split between H^+ and O^+ according to the relations of *Young et al.* [1982] (higher-energy observations were assumed to be H^+, other than a $\kappa = 5$ high-energy extension of the lower-energy O^+ distribution). The SOPA flux values above 75 keV were used for the H^+ boundary condition only. In between 40 keV and 75 keV for H^+, interpolation was made to match the two flux distributions. Thus the κ distribution was used differently for H^+ and O^+: only up to 75 keV for the former but for all energies for the latter. Loss mechanisms include the flow of plasma out the dayside outer boundary, precipitation of particles into the upper atmosphere, pitch angle scattering, and drag from Coulomb collisions (using the plasmaspheric model of *Ober et al.* [1997]), and charge exchange with the neutral hydrogen geocorona (using the model of *Rairden et al.* [1986]).

[36] The Volland-Stern electric field model was described in section 3.1. The self-consistent electric field uses the field-aligned currents (FACs) from the storm-time partial ring current as source terms in a Poisson equation solution for the subauroral potential structure (including a dynamically defined ionospheric conductance). The calculation is described in more detail by *Ridley and Liemohn* [2002] and *Ridley et al.* [2004]; initial results with this self-consistent

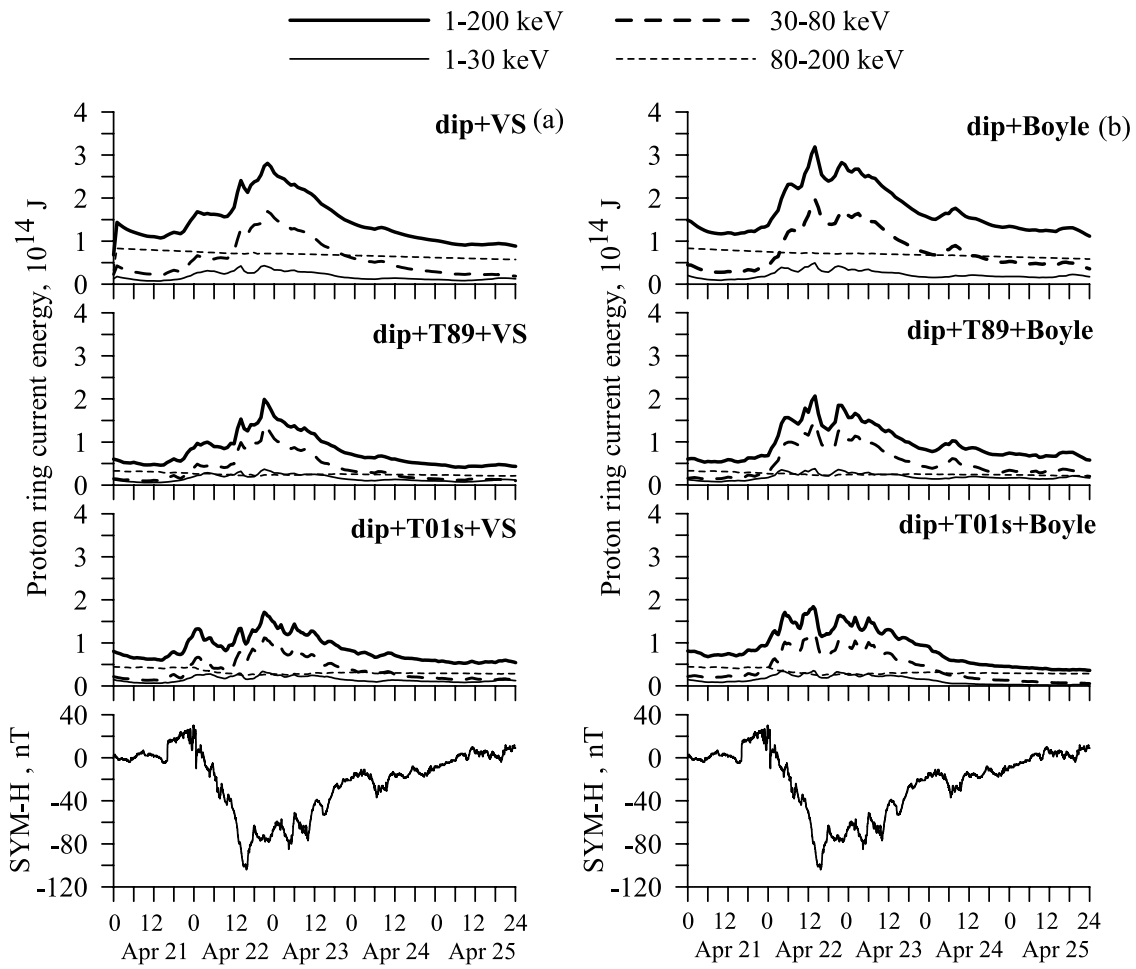

Figure 5. The 2001-04-21–25 storm, Ganushkina model, initial distribution filling the magnetosphere at the start of the tracing. Format is similar to that in Figure 3.

model were presented by *Liemohn et al.* [2004, 2005]. This field is similar to other self-consistent inner magnetospheric electric field calculations [*Spiro and Wolf*, 1984; *Fok et al.*, 2001; *Khazanov et al.*, 2003], with the primary difference being the chosen conductance pattern.

6. Model Results

6.1. Ganushkina Model: Influence of the Electric and Magnetic Fields

[37] Figure 3 shows the results for the proton ring current energy with several electric and magnetic field models, and with an empty magnetosphere as the initial condition. The four lines show the total (1–200 keV, thick solid lines), low (1–30 keV, thin solid lines), medium (30–80 keV, thick dashed lines), and high energies (80–200 keV, thin dashed lines). Tracing results using the Volland-Stern convection electric field are shown in the left panel, and tracing results using the Boyle et al. polar cap potential applied to Volland-Stern model are shown in the right panel. The magnetic field models are shown row by row, with dipole in the top row, Tsyganenko T89 in the second row, and Tsyganenko T01S in the third row. The plasma sheet number density and parallel and perpendicular temperatures were obtained from the LANL MPA particle measurements as described above.

[38] All profiles show an increase during the SYM-H decrease and a peak right after the SYM-H minimum. When tracing in the Kp-dependent Volland-Stern electric field and static dipole magnetic field (Figure 3a, top row), the maximum value for the total proton ring current energy was about 2 10^{14} J. Using a more realistic magnetic field model resulted in the decrease of the peak value to 1.7 10^{14} J for the Kp-dependent Tsyganenko T89 (Figure 3a, second row) and to 1.4 10^{14} J for the storm-time T01S model (Figure 3a, third row). Relative contributions from the protons in different energy ranges did not change much: Throughout the storm the main contribution came from the medium energy protons, whereas the high-energy protons gave the smallest contribution.

[39] Using the solar wind-driven Boyle et al. function for the polar cap potential (see section 3.2, Figure 3b) did not significantly change the results described above. That formulation of the electric field resulted in slightly higher values of the ring current energy content but did not influence the energy spectrum.

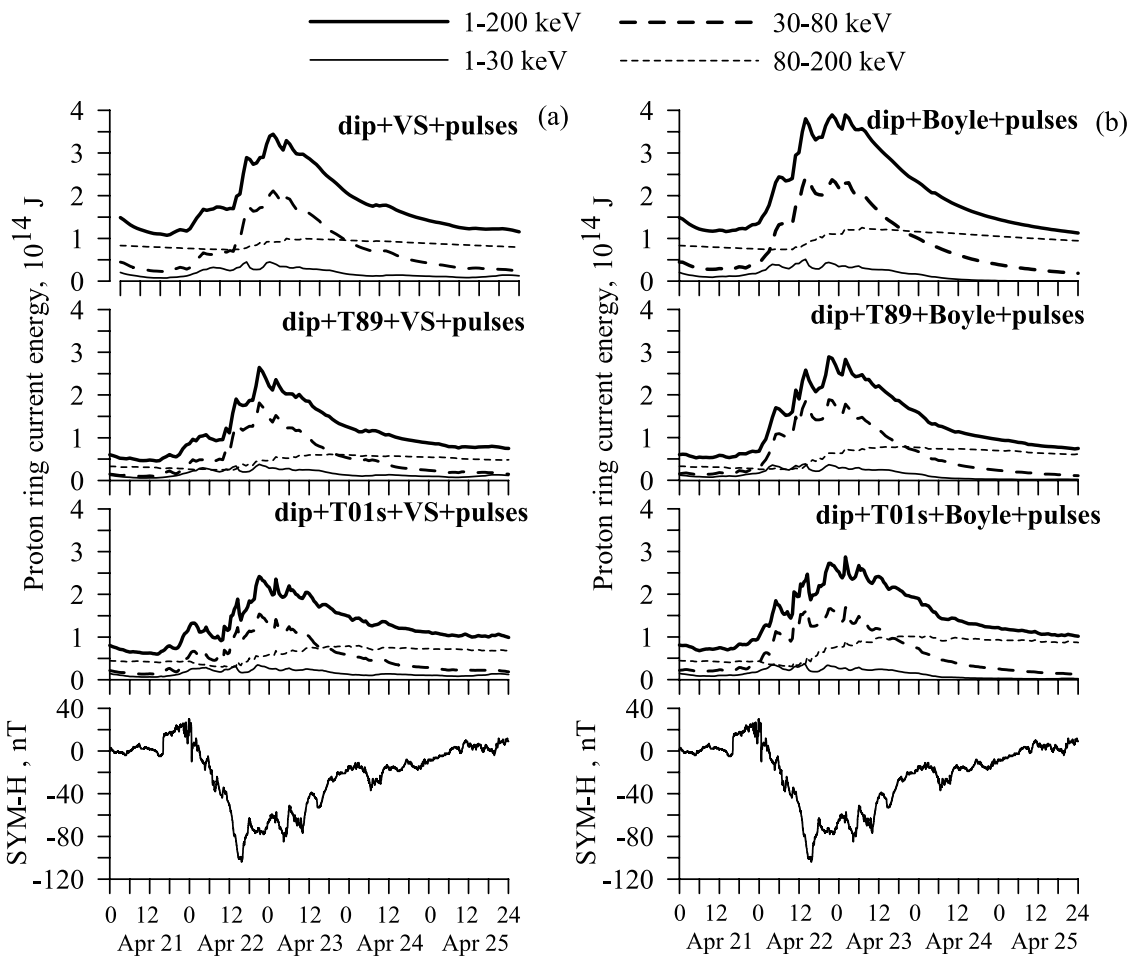

Figure 6. The 2001-04-21–25 storm, Ganushkina model, initial distribution filling the magnetosphere at the start of the tracing, electromagnetic pulses launched at substorm onset times. Format is similar to that in Figure 3.

6.2. Ganushkina Model: Role of Smaller-Scale Electric Fields

[40] Figure 4, similarly to Figure 3, shows the model proton ring current energies for the four energy ranges. The magnetosphere was initially empty and the boundary conditions were obtained from the LANL MPA particle measurements. The electric field models now included the substorm-associated pulses described in section 3.3.

[41] It is clear that the electromagnetic pulses led to highly efficient transport and energization of the protons into the inner magnetosphere. The resulting energy profile is such that the dominant contribution to the ring current comes from the high-energy protons during the recovery phase, in addition to an overall increase in the total proton ring current energy.

6.3. Ganushkina Model: Effects of the Initial Distribution

[42] Figure 5 shows the proton ring current energy for the four energy ranges calculated as in Figure 3 but with an initial distribution instead of empty magnetosphere before tracing. The modeling with an initially filled inner magnetosphere resulted in an increase by a factor of about 1.7 of the total proton ring current energy. In general, the ring current energy distribution did not change much, except for the high energies: Their contribution was dominant before the storm and did not change much during the storm, while during the storm main phase and early recovery there was a significant increase of the contribution from medium-energy protons. High-energy protons did become dominant during the late recovery phase. This change occurred because of the almost constant contribution of the high-energy population and the rapidly decreasing population of the medium-energy protons. Thus there was no net increase of the high-energy population during the recovery phase. Low-energy protons were still the least important contributor to the ring current energy.

[43] Figure 6 shows the proton ring current energy for the four energy ranges with initial distribution, similar to that used to produce Figure 5 but with the addition of electromagnetic pulses at substorm onsets similar to Figure 4. Owing to the initial distribution, the high-energy protons are dominant before the storm. The storm main phase was characterized by the increase and dominance of medium energy protons and a small decrease of the high-energy protons. At the beginning of the recovery phase, the contribution from the medium-energy protons started to decrease, whereas there was a clear increase in the high-energy

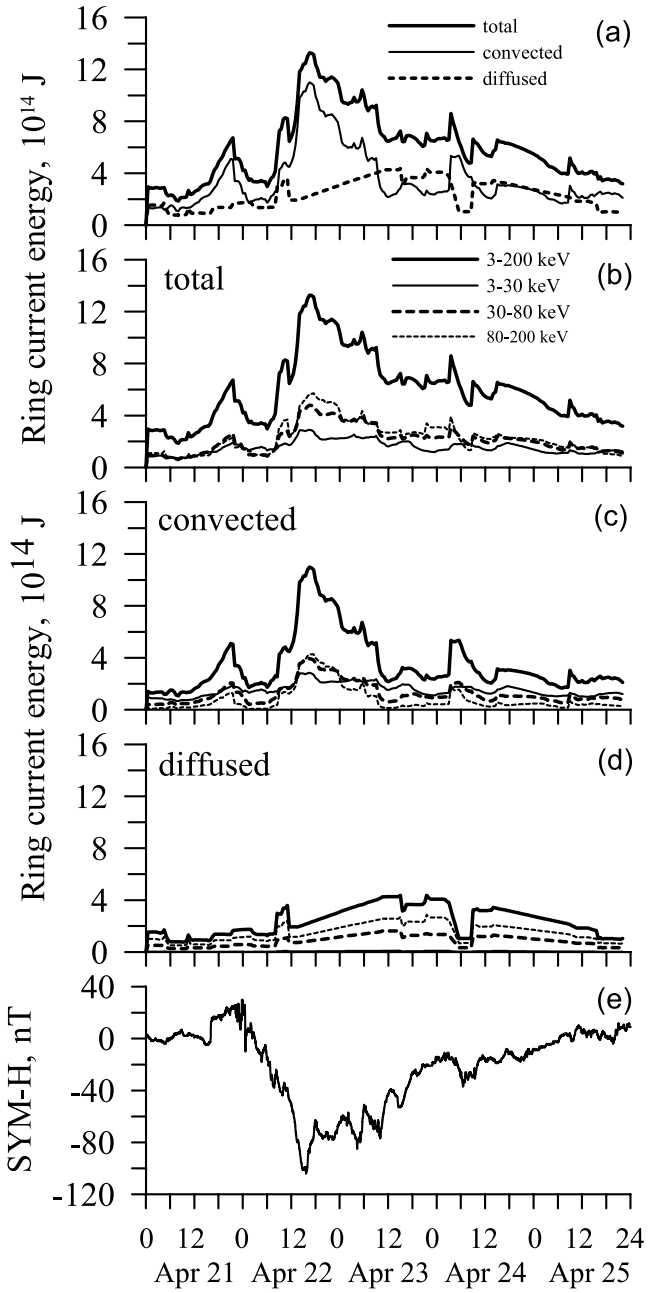

Figure 7. The 2001-04-21–25 storm, Milillo model: the evolution of the proton ring current energy computed from the empirical model of inner magnetospheric proton distributions by *Milillo et al.* [2006]. (a) Protons with energies of 3–200 keV, total energy (thick solid line), convected/injected population (thin solid line), and the diffused population (dashed line). The evolution of proton ring current in four energy ranges, 3–200 keV (thick solid line), 3–30 keV (thin solid line), 30–80 keV (thick dashed line), and 80–200 keV (thin dashed line) for (b) the global magnetospheric population, (c) the convected/injected population and (d) the diffused population. (e) SYM H index.

contribution, which led to the dominance of high-energy protons during the late recovery.

6.4. Milillo Model: Proton Ring Current Energy Evolution

[44] The total energy content between 3 and 7 R_E from the *Milillo et al.* [2003, 2006] model is plotted in Figure 7a for energies between 3 and 200 keV with the thick solid line (note that the scales are different than in the earlier figures). The contributions of the convected/injected (thin solid line) and the diffused (dashed line) populations are shown separately. The total energy content matches quite well the SYM-H index behavior shown in Figure 7e. The major contribution during the storm main phase comes from the convected/injected particles. During the storm recovery this contribution rapidly decreases while the energy of the diffused particle population strongly increases.

[45] Figure 7 also shows the total energy computed for protons with energies of 3–200 keV (thick solid line), 3–30 keV (thin solid line), 30–80 keV (thick dashed line), and 80–200 keV (thin dashed line) for the total magnetospheric distribution (Figure 7b), the convected/injected population (Figure 7c), and the diffused population (Figure 7d). The diffused population generally has a peak at energies higher than 80 keV, while the convected/injected population has more even contribution from all energy ranges. Figure 7b shows that the major contribution to the total energy content comes from the highest energy range not only during the storm recovery phase, but also during the main phase. Conversely, Figures 7c and 7d reveal that the major contribution during the main phase is due to the convection/injection population.

6.5. Liemohn Model

[46] Figure 8 presents the output from the RAM model in a dipole magnetic field and with a Volland-Stern electric field (Figure 8a) and a self-consistent electric field (Figure 8b) as the evolution of ring current energy for particles with all energies (thick solid line) and for low (1–30 keV, thin solid line), medium (30–80 keV, thick dashed line), and high (>80 keV, thin dashed line) energies together with SYM-H index (Figure 8c) for three days of the 2001-04-21–23 storm.

[47] Figures 8a and 8b show that these RAM simulations used a dominating initial condition for the high-energy protons in the inner magnetosphere. The medium- and low-energy ranges are essentially zero at the beginning of the runs. The time history of the total energy content for all protons in the inner magnetosphere is shown by the solid curves in Figures 8a and 8b. The total energy content curve from the Volland-Stern simulation (Figure 8a) shows the main peak occurring 8 hours later than the SYM-H minimum, and it does not reproduce any of the smaller-scale features. The self-consistent electric field result (Figures 8b) reproduces the first two minima of the SYM-H curve very well (in both timing and relative magnitude) and also includes hints of the later local minima in SYM-H. Thus it seems that the self-consistent electric field is a clear improvement over the Volland-Stern electric field model.

[48] As the storm main phase begins, both simulations show a slow decrease in the energy content of the >80 keV protons. The Volland-Stern electric field produces several mild increases in the content of this energy range, particularly

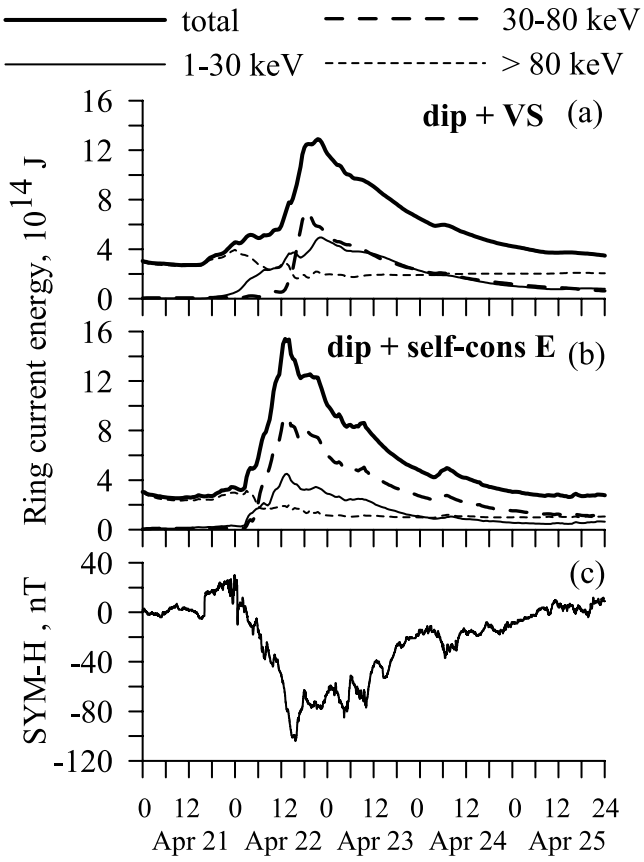

Figure 8. The 2001-04-21–23 storm, results from the RAM model: the evolution of ring current energy in units of 10^{14} J for particles with all energies (thick solid line), and for low (1–30 keV, thin solid line), medium (30–80 keV, thick dashed line), and high (>80 keV, thin dashed line) energies calculated as the output from the RAM [*Liemohn et al.*, 2001] in dipole magnetic field and in (a) Volland-Stern electric field and (b) self-consistent electric field. (c) Dst index.

near the storm peak, but overall the simulation resulted in a net loss of energy content. The self-consistent electric field did not produce any such enhancement in the high-energy proton contribution and instead simply shows a steadily decreasing energy content in this high-energy range. During the recovery phase, the contribution from these protons is essentially constant in both simulations.

[49] The medium-energy range (30–80 keV) shows the largest enhancement during the storm simulations. After a rapid initial increase, the two electric field models produce peak values of 4.3 10^{14} J and 5.6 10^{14} J, respectively. Both simulations then show a slow decrease of the contribution from this energy range to the end-of-simulation values of 0.4 10^{14} J and 0.7 10^{14} J, respectively.

[50] The low-energy protons (1–30 keV) contribute the less than the medium energies to the total energy content for both simulations. The contribution from this range rises slowly in the Volland-Stern field, peaking with the total energy content peak late on 22 April and then slowly decreasing throughout the recovery phase. In the self-consistent electric field, the rise is faster but the peak value is similar, and the recovery phase decline is also very similar to that of the analytical electric field result.

[51] The RAM simulation predicts that the bulk of the proton energy content during the storm main phase and early recovery phase is carried by particles with energies of 80 keV or less. The high-energy protons are not enhanced during the recovery phase of the storm; their relative contribution to the total energy content rises but only because the contributions from the other energy ranges are decreasing during this interval.

7. Discussion

[52] In this paper we present results from three different ring current models run for the GEM storm on 2001-04-21–25. While all models reproduce the enhancement of the ring current as Dst drops to storm values, the details of the model results vary from model to model and within each model depending on the initial and boundary conditions and empirical parametrizations used. Here we discuss observational constraints and compare and contrast the model results with each other.

[53] Earlier statistical results by *Ganushkina et al.* [2005] showed that before the storm the main contribution to the ring current energy comes from high-energy protons having energies exceeding about 80 keV. Medium-energy protons (30–80 keV) contribute somewhat less, and the smallest part comes from low-energy protons (below 30 keV). A storm main phase results in an increase of total energy with clear dominance of medium-energy protons, smaller increase of low-energy protons, and slight decrease of high-energy protons. The recovery phase is characterized by a significant growth of the contribution from the high-energy protons with an evident decrease of the contributions from medium and low energies. At the end of the recovery phase, the high-energy protons dominate over medium and low energies.

[54] The values obtained from the Polar MICS instrument for the 2001-04-21–25 storm were smaller by a factor of ten (see Figure 1) as compared to the average statistical results. Another difference was the large contribution from low-energy protons that was not present in the statistics by *Ganushkina et al.* [2005]. The differences between the observations in this event and the statistical results can be explained by the orbital evolution of the Polar spacecraft: By 2001, the Polar orbit had evolved so that the crossing of the ring current L-shells was rather fast and the crossings occurred at relatively high magnetic latitudes. Assuming that the pitch angle distribution does not change when mapping the observed fluxes into the equatorial plane leads to an underestimation of the fluxes; earlier observational and modeling studies suggest that the high-energy portion of the distributions falls off faster than the low-energy part when moving to higher latitudes [*Fok et al.*, 1996; *Chen et al.*, 1998]. Thus it is likely that the high-energy contribution observed by Polar is an underestimate, and thus the dominance of the low-energy particles is an artefact produced by the measurement location.

[55] The proton energy distributions were modeled by tracing protons in the drift approximation in different time-dependent magnetic and electric fields [*Ganushkina et al.*, 2005]. The effect of changing the magnetic field model from dipolar to tail-like (T89) to storm-time (T01s) in all cases led

to decreasing energy content of the ring current. This decrease occurs because the more realistic field models produce a smaller equatorial field in the inner magnetosphere, which moves the trapping boundary closer to the Earth and causes more particles to drift around the Earth and get lost at the magnetopause. Similarly, the more realistic magnetopause location (not present in a dipole) moving inward due to high solar wind pressure compression leads to more particles interacting with the magnetopause and not reaching trapped orbits. Last, the smaller field gradients lead to smaller adiabatic energy gain of the particles. Changing from a dipole to a storm-time magnetic field model caused a decrease in the ring current energy by about 30%.

[56] The errors of the order of 30% highlight the importance of selecting an appropriate magnetic field model for each event. While the statistical empirical models can give quite a good representation of the field, it is still important to verify by comparison with in situ measurements that the field model is indeed accurately reflecting the storm dynamics. Especially during large storms, the field can be considerably different from the statistical average; during such periods event-oriented methods that allow tuning of the field models to best correspond to observations should be utilized [*Ganushkina et al.*, 2004].

[57] Change of the electric field model from the Volland-Stern model to the Boyle et al. function for the polar cap potential did not change the large-scale ring current behavior much. Both the peak energy density and the energy spectrum (or energy content in the different energy ranges) were quite similar for the two models. The solar wind-driven changes in the potential pattern reproduce some finer-scale changes in the temporal behavior better than the 3-hour-averaged convection, but the overall result of the ring current buildup and decay were quite similar for both electric field models. Note that the Liemohn model predicts somewhat (but not significantly) larger effects between different convection electric field models. This is because the Liemohn model uses a dipole field as the magnetic field model, which reduces the relative effect of the magnetic drifts on the particle trajectories.

[58] Introduction of the electromagnetic pulses to the electric field models led to a marked increase of the peak energy by over 30%. The pulses also had a significant effect on the energy distribution: They caused largest increase in the highest energy range, leading to a ring current energy spectrum that best corresponds to the statistical results [*Ganushkina et al.*, 2005]. While initial filling of the inner magnetosphere with high-energy particles leads to similarly enhanced total energy density, the increase of the high-energy end of the ring current was only obtained through inclusion of the smaller-scale, localized pulses at substorm onset times.

[59] The empirical model of the inner magnetospheric proton distributions [*Milillo et al.*, 2001] allows one to follow the total, convected/injected, and diffused populations separately [*Milillo et al.*, 2006]. The model result predicted a major contribution during the storm main phase from the convected/injected particles. During the storm recovery this contribution rapidly decreased with the simultaneous increase of the contribution from the diffused particles. The peak energy content in this model was about three times as large as in the Ganushkina model.

[60] The energy distribution during the storm in the Milillo model stayed approximately constant in time: Throughout the storm, the energy contents in the high and medium energies were almost equal, with lowest energy content in the low-energy particles. However, separation of the convected and diffused populations shows that for the diffused population, the energy content is dominated by the high-energy particles with hardly any energy density in the lowest energy range below 30 keV. Neither the convected nor the diffused population showed any change in the energy spectrum during the course of the storm, and the storm ended with equal partitioning of the energy content between the three energy ranges.

[61] The emphasis on high-energy end of the energy spectrum can be naturally explained by the model properties: First, linear interpolation of the diffused population parameters during the main phase (when there were no observations to constrain the model) leads to an overestimation of their intensity. Second, it seems that also the spectra of the convected population overestimate the highest energy range. Comparison of the observed spectra and the spectra obtained from the fitting shows that they agree very well close to the peak, but that at higher energies the model spectra show larger fluxes [see *Milillo et al.*, 2006, Figure 12]. This is an intrinsic limitation of a method based on fitting the energy spectra in a logarithmic scale. This means that especially during the storm main phase the spectral profiles are not well described by simple Gaussians, as the fluxes drop steeply at higher energies. While this effect does not change the global trend of the model results, it does indicate that at energies above 80 keV the model may produce an overestimation of the fluxes of the convected/injected particles especially during storm main phases. The rapid dropout of high-energy fluxes may be caused by opening of particle trajectories at higher energies, which causes the highest-energy source population to escape from the magnetosphere, never reaching the inner magnetosphere. A further limitation of the empirical method is that it assumes conservation of the global shape of the proton distributions. While this assumption seems to be globally valid [*Orsini et al.*, 2004; *Milillo et al.*, 2006], it can fail locally during transient processes not included or not statistically significant in the data set used to produce the empirical model [*Milillo et al.*, 2006].

[62] A direct solution of the Boltzmann equation for the phase space density throughout the inner magnetosphere using the RAM code [*Liemohn et al.*, 2001, 2004] was obtained using two choices for the electric field description: the analytically defined Volland-Stern potential model driven by Kp, and a self-consistent electric field calculation within the RAM model. The RAM code predicts the following time sequence for the proton ring current energy content: Before the storm, the high-energy channel dominates the total energy content of the ring current protons. During the main phase, the medium energy protons exhibit a rapid enhancement, eventually dominating over the high-energy proton contribution. In the Volland-Stern simulation, this dominance is short-lived. In the self-consistent simulation, however, this dominance lasts much longer. Eventually, during the recovery phase, the medium energy protons degrade and the high-energy protons regain an equal contribution to the total energy content. In the Volland-Stern simulation there is lesser acceleration of the medium-energy particles, leaving the

highest energies dominant at the end of the simulation. The peak energy content values from the Liemohn model are quite comparable with those from the Milillo model, but again about a factor of three larger than the Ganushkina model results.

[63] The high-energy proton content during the main phase is highly dependent on the initial condition, and thus the choice of a large prestorm content significantly affects the final energy distribution. That is, smaller high-energy fluxes in the initial condition would result in their smaller relative contribution at the end of the simulation, as their energy content slowly decreases throughout the run. The late-recovery-phase increase in the energy content of the high-energy protons is not present in the RAM simulation.

[64] The differences in the model results and their limited reproduction of the statistically observed results can be at least partially be attributed to the limitations in the numerical approaches. In the following, we address a few key uncertainties in the three models.

[65] Of the three models, only the RAM simulation considers the higher-mass ring current particles, which are known to be even dominant during some storms. The Polar measurements indicate that this storm was dominated by protons, this is also consistent with the predictions by the *Young et al.* [1982] formulas. For instance, the CAMMICE/MICS summary plots (not shown) show that the H^+ count rate was over an order of magnitude higher than that for O^+. Similarly, the RAM simulations had at most 30% of the total energy content of the ring current in O^+ (near the peak of the storm), and before and after the storm this percentage was much smaller. For cases where the energy density is dominated by the heavier ions, their contribution needs to be carefully examined and accounted for.

[66] The boundary conditions derived from the Los Alamos MPA measurements involve another source of error, uncertainty, and variability. The Ganushkina model uses the moments computed from the MPA data and assumes a κ distribution at the boundary. A similar approach was used in the Liemohn model for these model runs. The Milillo model utilizes a larger energy range by including both MPA and SOPA energies in fitting to a Gaussian function. Thus even using the same data to define the boundary conditions, each model starts with a different proton distribution at the outer boundary. While a κ distribution sometimes is a good representation of the nightside geosynchronous plasma energy spectrum [e.g., *Christon et al.*, 1991], at other times it is not (M. Thomsen, private communication, 2006). A full measured spectrum from the MPA instrument in this case gave more particles at the very low and very high energy ranges than was estimated by a kappa function. The differences in the measured and fitted spectra clearly indicate that the boundary conditions need to be carefully specified using as full knowledge of the distribution as possible.

[67] Another assumption of the numerical approaches is that the same pitch angle anisotropy is used for all energies at the outer simulation boundaries of the models. These assumptions are slightly different between the models, with the Ganushkina and Liemohn models using a bi-kappa distribution and the Milillo model using an isotropic boundary condition, but the resulting limitation is the same. That is, the true distribution most likely has a pitch angle anisotropy that varies with energy [*Fok et al.*, 1996; *Chen et al.*, 1998]. Coulomb collisions, for instance, scatter the lower-energy particles faster than the higher-energy particles because the plasmaspheric electrons with characteristic energies less than 1 eV resonate most efficiently with protons in the 1–10 keV range [*Fok et al.*, 1991]. Electromagnetic ion cyclotron waves will interact with all particles but will cause larger precipitation fluxes for the lower-energy particles [*Jordanova et al.*, 2001b]. Implementing an energy-dependent pitch angle distribution for the outer boundary proton fluxes is therefore another step that we need to consider in the future.

[68] The model results can be compared with the Dst or SYM-H measurements by converting the peak energy values to magnetic perturbations at the Earth's surface using the Dessler-Parker-Sckopke (DPS) formulation [*Dessler and Parker*, 1959; *Sckopke*, 1966]. This formulation relates the total energy within the ring current particles to a magnetic disturbance at Earth using $\Delta B = 3.98\ 10^{-30}\ E_{RC}$ [e.g., *Liemohn*, 2003]. Using the peak values of $4\ 10^{14}$ J for the Ganushkina model and $14\ 10^{14}$ J for the Milillo and Liemohn models gives ground disturbances of only 10 and 35 nT, respectively, while the observed Dst disturbance was of the order of 100 nT. Thus it seems that all models significantly underestimate the total energy content in the ring current region as predicted by the DPS relationship. This may either be because the models do not provide enough energy content in the inner magnetosphere, or, alternatively, because the DPS formulation does not accurately account for effects such as the tail, magnetopause, or ground-induced currents that contribute to the Dst measurements. Note that the energy content time series presented in this study are for H^+ only, and O^+ will increase the simulated ring current energy content (although by less than a factor of 2, as H^+ is thought to be dominant throughout this storm).

[69] The electric field models used here are still at their infancy. The Ganushkina model used a simple Kp-driven Volland-Stern convection model as well as a model based on ionospheric potential driven by the solar wind and IMF parameters mapped to the magnetotail. Both convection models were shielded from the inner magnetosphere. The Liemohn model uses a self-consistent electric field that includes modification of the inner magnetospheric electric field pattern due to closure of the storm-time partial ring current *Liemohn et al.*, 2004, 2005]. Similarly to results suggested by the *Rowland and Wygant* [1998] study, in that case shielding may not be present during strong activity, and the intensity of the large-scale convection field increases as the radial distance from the Earth decreases. However, this does not lead to an increase of the ring current energy content, as the enhanced electric field at small L values more effectively kicks out the preexisting high-energy ring current, while the suppressed E at larger L values more effectively inhibits the injection of fresh protons to the high-energy range. On the other hand, this study showed that the electric fields need to be pulsed and localized to provide acceleration preferentially for the high-energy population. Only such electric fields could provide the observed change in the energy content distribution in the ring current from medium-energy dominance during the main phase to the high-energy dominance during the recovery phase. Modeling of the electric field, in a way that it would be self-consistent with the time-evolving magnetic field, remains one of the large challenges for inner magnetosphere modeling.

8. Conclusions

[70] Comparison of three ring current models using various parametrizations leads us to the following conclusions:

[71] 1. Changing the magnetic field model from dipole to a more realistic one decreases the ring current energy content by about 30%. This result is quite independent of the model details and is a consequence of increased amount of open drift trajectories as well as smaller amount of adiabatic energization.

[72] 2. The details of the convection electric field cause small-scale changes in the time-evolution of the ring current energy content, but overall the changes are small and do not change the energy spectrum of the ring current. While increasing convection strength can bring substantial amounts of ring current ions to the inner magnetosphere, time-dependent and localized electric fields are the only means to provide preferential increase of the energy content of the high-energy particles.

[73] 3. Examining the convected and diffused populations separately suggest that the role of the diffusion processes in bringing in ring current ions is relatively small (of the order of 30% or less) during the storm main phase, while during the recovery phase the role of diffusion increases such that the relative contributions of convection and diffusion to the energy content are almost equal.

[74] 4. The initial population in the inner magnetosphere and the plasma populations used as boundary conditions have significant effects on the model results. Thus better data from missions like the Radiation Belt Storm Probes (RBSP) or the Outer Radiation Belt Injection, Transport, Acceleration and Loss Satellite (ORBITALS) are vital for better understanding of the inner magnetosphere dynamics.

[75] The results in this paper highlight the importance of investigating the high-energy end of the ring current population. It was shown that the electric field pulses significantly increase the energy of the ring current particles, up to several hundred keV, and even above. These diffused particles gain sufficient energy to become significant also for humans and/or technological systems in space. Thus it is vital to include all acceleration processes that are significant in producing these populations as well as to encompass the entire energy range in ring current modeling efforts.

[76] **Acknowledgments.** We thank M. Thomsen for providing the LANL MPA data and for useful comments on the manuscript and S. Orsini for useful discussions. We thank T. Fritz for the use of the Polar CAMMICE/MICS and D. McComas and C. Smith for the ACE plasma and magnetic field data, which were obtained through the CDAWeb data distribution system operated and maintained by the NSSDC. The geomagnetic indices were obtained from the World Data Center in Kyoto. TP thanks the IGPP for hosting her visit to the Los Alamos National Laboratory. ML thanks NASA and NSF for funding to participate in this study.

[77] Amitava Bhattacharjee thanks the reviewers for their assistance in evaluating this paper.

References

Aggson, T. L., J. Heppner, and N. Maynard (1983), Observations of large magnetospheric electric fields during the onset phase of a substorm, *J. Geophys. Res.*, *88*, 3981.

Angelopoulos, V., et al. (1992), Bursty bulk flows in the inner central plasma sheet, *J. Geophys. Res.*, *97*, 4027.

Bame, S. J., et al. (1993), Magnetospheric plasma analyzer for spacecraft with constrained resources, *Rev. Sci. Instr.*, *64*, 1026.

Baumjohann, W., G. Paschmann, and H. Luehr (1990), Characteristics of high-speed ion flows in the plasma sheet, *J. Geophys. Res.*, *95*, 3801.

Belian, R. D., G. R. Gisler, T. Cayton, and R. Christensen (1992), High-Z energetic particles at geostationary orbit during the great solar proton event series of October 1989, *J. Geophys. Res.*, *97*, 16,897.

Boyle, C. B., P. H. Reiff, and M. R. Hairston (1997), Empirical polar cap potentials, *J. Geophys. Res.*, *102*, 111.

Chen, M. W., J. L. Roeder, J. F. Fennell, L. R. Lyons, and M. Schultz (1998), Simulations of ring current proton pitch-angle distributions, *J. Geophys. Res.*, *103*, 165.

Christon, S. P., D. J. Williams, D. G. Mitchell, C. Y. Huang, and L. A. Frank (1991), Spectral characteristics of plasma sheet ion and electron populations during disturbed geomagnetic conditions, *J. Geophys. Res.*, *96*, 1.

Dessler, A. J., and E. N. Parker (1959), Hydromagnetic theory of geomagnetic storms, *J. Geophys. Res.*, *64*, 2239.

Ebihara, Y., and M. Ejiri (2000), Simulation study on fundamental properties of the storm-time ring current, *J. Geophys. Res.*, *105*, 15,843.

Ebihara, Y., and M. Ejiri (2003), Numerical simulation of the ring current: Review, *Space Sci. Rev.*, *105*, 377.

Fok, M.-C., J. U. Kozyra, A. F. Nagy, and T. E. Cravens (1991), Lifetime of ring current particles due to Coulomb collisions in the plasmasphere, *J. Geophys. Res.*, *96*, 7861.

Fok, M.-C., J. U. Kozyra, G. C. Ho, and D. C. Hamilton (1995), Three-dimensional ring current decay model, *J. Geophys. Res.*, *100*, 9619.

Fok, M.-C., T. E. Moore, and M. E. Greenspan (1996), Ring current development during storm main phase, *J. Geophys. Res.*, *100*, 15,311.

Fok, M.-C., T. E. Moore, and D. C. Delcourt (1999), Modeling of inner plasma sheet and ring current during substorms, *J. Geophys. Res.*, *104*, 14,557.

Fok, M.-C., R. A. Wolf, R. W. Spiro, and T. E. Moore (2001), Comprehensive computational model of the Earth's ring current, *J. Geophys. Res.*, *106*, 8417.

Ganushkina, N. Y., and T. I. Pulkkinen (2002), Particle tracing in the inner Earth's magnetosphere and the formation of the ring current during storm times, *Adv. Space Res.*, *30*, 1817.

Ganushkina, N. Y., T. I. Pulkkinen, and V. A. Sergeev, et al. (2000), Entry of plasma sheet particles into the inner magnetosphere as observed by Polar/CAMMICE, *J. Geophys. Res.*, *105*, 25,205.

Ganushkina, N. Y., T. I. Pulkkinen, V. F. Bashkirov, D. N. Baker, and X. Li (2001), Formation of intense nose structures, *Geophys. Res. Lett.*, *28*, 491.

Ganushkina, N. Y., T. I. Pulkkinen, M. V. Kubyshkina, H. J. Singer, and C. T. Russell (2004), Long-term evolution of magnetospheric current systems during storms, *Ann. Geophys.*, *22*, 1317.

Ganushkina, N. Y., T. I. Pulkkinen, and T. Fritz (2005), Role of substorm-associated impulsive electric fields in the ring current development during storms, *Ann. Geophys.*, *23*, 579.

Hedin, A. E. (1991), Extension of the MSIS thermosphere model into the middle and lower atmosphere, *J. Geophys. Res.*, *96*, 1159.

Janev, R. K., and J. J. Smith (1993), Cross sections for collision processes of hydrogen atoms with electrons, protons, and multiply-charged ions, in *Atomic and Plasma Material Interaction Data for Fusion*, vol. 4, pp. 78–79, Int. At. Energ. Agency, Vienna.

Jordanova, V. K., L. M. Kistler, C. J. Farrugia, and R. B. Torbert (2001a), Effects of inner magnetospheric convection on ring current dynamics: March 10–12, 1998, *J. Geophys. Res.*, *106*, 29,705.

Jordanova, V. K., C. J. Farrugia, R. M. Thorne, G. W. Khazanov, G. D. Reeves, and M. F. Thomsen (2001b), Modeling ring current proton precipitation by electromagnetic ion cyclotron waves during the May 14–16, 1997, storm, *J. Geophys. Res.*, *106*, 7.

Khazanov, G. V., M. W. Liemohn, T. S. Newman, M.-C. Fok, and R. W. Spiro (2003), Self-consistent magnetosphere-ionosphere coupling: Theoretical studies, *J. Geophys. Res.*, *108*(A3), 1122, doi:10.1029/2002JA009624.

Khazanov, G. V., M. W. Liemohn, T. S. Newman, M.-C. Fok, and A. J. Ridley (2004a), Magnetospheric convection electric field dynamics and stormtime particle energization: Case study of the magnetic storm of 4 May 1998, *Ann. Geophys.*, *22*, 497.

Khazanov, G. V., M. W. Liemohn, M.-C. Fok, T. S. Newman, and A. J. Ridley (2004b), Stormtime particle energization with high temporal resolution AMIE potentials, *J. Geophys. Res.*, *109*, A05209, doi:10.1029/2003JA010186.

Kozyra, J. U., et al. (1998), Effects of a high-density plasma sheet on ring current development during the November 2–6, 1993, *J. Geophys. Res.*, *103*, 26,285.

Lee, L. C., G. Corrick, and S.-I. Akasofu (1983), On the ring current energy injection rate, *Planet. Space Sci.*, *31*, 901.

Li, X., et al. (1998), Simulation of dispersionless injections and drift echoes of energetic electrons associated with substorms, *Geophys. Res. Lett.*, *25*, 3763.

Liemohn, M. W. (2003), Yet another caveat to using the Dessler-Parker-Sckopke relation, *J. Geophys. Res.*, *108*(A6), 1251, doi:10.1029/

2003JA009839.
Liemohn, M. W., J. U. Kozyra, V. K. Jordanova, G. V. Khazanov, M. F. Thomsen, and T. E. Cayton (1999), Analysis of early phase ring current recovery mechanisms during geomagnetic storms, *Geophys. Res. Lett.*, *26*, 2845.
Liemohn, M. W., et al. (2001), Dominant role of the asymmetric ring current in producing the stormtime Dst, *J. Geophys. Res.*, *106*, 10,883.
Liemohn, M. W., A. J. Ridley, D. L. Gallagher, D. M. Ober, and J. U. Kozyra (2004), Dependence of plasmaspheric morphology on the electric field description during the recovery phase of the April 17, 2002 magnetic storm, *J. Geophys. Res.*, *109*, A03209, doi:10.1029/2003JA010304.
Liemohn, M. W., A. J. Ridley, P. C. Brandt, D. L. Gallagher, J. U. Kozyra, D. G. Mitchell, E. C. Roelof, and R. DeMajistre (2005), Parametric analysis of nightside conductance effects on inner magnetospheric dynamics for the 17 April 2002 storm, *J. Geophys. Res.*, *110*, A12S22, doi:10.1029/2005JA011109.
Maynard, N. C., and A. J. Chen (1975), Isolated cold plasma regions: Observations and their relation to possible production mechanisms, *J. Geophys. Res.*, *80*, 1009.
Maynard, N. C., et al. (1996), Dynamics of the inner magnetosphere near times of substorm onsets, *J. Geophys. Res.*, *101*, 7705.
McIlwain, C. E. (1986), A *Kp*-dependent equatorial electric field model, *Adv. Space Res.*, *6*, 187.
Milillo, A., S. Orsini, and I. A. Daglis (2001), Empirical model of proton fluxes in the equatorial inner magnetosphere: 1. Development, *J. Geophys. Res.*, *106*, 25,713.
Milillo, A., S. Orsini, D. C. Delcourt, A. Mura, S. Massetti, E. De Angelis, and Y. Ebihara (2003), Empirical model of proton fluxes in the equatorial inner magnetosphere: 2. Properties and applications, *J. Geophys. Res.*, *108*(A5), 1165, doi:10.1029/2002JA009581.
Milillo, A., S. Orsini, A. Mura, and S. Massetti (2006), Geomagnetic activity dependence of the inner magnetospheric proton distribution: An empirical approach for the 21–25 April 2001 storm, *J. Geophys. Res.*, doi:10.1029/2006JA011956, in press.
Ober, D. M., J. L. Horwitz, and D. L. Gallagher (1997), Formation of density troughs embedded in the outer plasmasphere by subauroral ion drift events, *J. Geophys. Res.*, *102*, 14,595.
Orsini, S., A. Milillo, and A. Mura (2004), Modeling of the inner magnetospheric time-evolving plasma: An empirical approach based on proton distribution, *J. Geophys. Res.*, *109*, A11216, doi:10.1029/2004JA010532.
Pulkkinen, T. I., et al. (2001), Ring current ion composition during solar minimum and rising solar activity: Polar/CAMMICE/MICS results, *J. Geophys. Res.*, *106*, 19,131.
Rairden, R. L., L. A. Frank, and J. D. Craven (1986), Geocoronal imaging with Dynamics Explorer, *J. Geophys. Res.*, *91*, 13,613.
Ridley, A. J., and M. W. Liemohn (2002), A model-derived description of the penetration electric field, *J. Geophys. Res.*, *107*(A8), 1151, doi:10.1029/2001JA000051.
Ridley, A. J., T. I. Gombosi, and D. L. De Zeeuw (2004), Ionospheric control of the magnetosphere: Conductance, *Ann. Geophys*, *22*, 567.
Roederer, J. G. (1970), *Dynamics of Geomagnetically Trapped Radiation*, 36 pp., Springer, New York.
Rowland, D. E., and J. R. Wygant (1998), Dependence of the large-scale, inner magnetospheric electric field on geomagnetic activity, *J. Geophys. Res.*, *103*, 14,959.
Sarris, T. E., X. Li, N. Tsaggas, and N. Paschalidis (2002), Modeling energetic particle injections in dynamic pulse fields with varying propagation speeds, *J. Geophys. Res.*, *107*(A3), 1033, doi:10.1029/2001JA900166.
Sckopke, N. (1966), A general relation between the energy of trapped particles and the disturbance field over the Earth, *J. Geophys. Res.*, *71*, 3125.
Sergeev, V. A., V. Angelopoulos, J. T. Gosling, C. A. Cattell, and C. T. Russell (1996), Detection of localized, plasma-depleted flux tubes or bubbles in the midtail plasma sheet, *J. Geophys. Res.*, *101*, 10,817.
Sheldon, R. B., and D. C. Hamilton (1993), Ion transport and loss in the Earth's quiet ring current: 1. Data and standard model, *J. Geophys. Res.*, *98*, 13,491.
Shiokawa, K., W. Baumjohann, and G. Haerendel (1997), Braking of high-speed flows in the near-Earth tail, *Geophys. Res. Lett.*, *24*, 1179.
Spiro, R. W., and R. A. Wolf (1984), Electrodynamics of convection in the inner magnetosphere, in *Magnetospheric Currents, Geophys. Monogr. Ser.*, vol. 28, edited by T. A. Potemra. p. 247, AGU, Washington, D. C.
Stern, D. P. (1975), The motion of a proton in the equatorial magnetosphere, *J. Geophys. Res.*, *80*, 595.
Takahashi, S., T. Iyemori, and M. Takeda (1990), A simulation of the storm-time ring current, *Planet. Space Sci.*, *38*, 1133.
Tsyganenko, N. A. (1989), A magnetospheric magnetic field model with a warped tail current sheet, *Planet. Space Sci.*, *37*, 5.
Tsyganenko, N. A. (2002a), A model of the near magnetosphere with a dawn-dusk asymmetry: 1. Mathematical structure, *J. Geophys. Res.*, *107*(A8), 1179, doi:10.1029/2001JA000219.
Tsyganenko, N. A. (2002b), A model of the near magnetosphere with a dawn-dusk asymmetry: 2. Parameterization and fitting to observations, *J. Geophys. Res.*, *107*(A8), 1176, doi:10.1029/2001JA000220.
Tu, J.-N., K. Tsuruda, H. Hayakawa, A. Matsuoka, T. Mukai, I. Nagano, and S. Yagitani (2000), Statistical nature of impulsive electric fields associated with fast ion flow in the near-Earth plasma sheet, *J. Geophys. Res.*, *105*, 18,901.
Volland, H. (1973), A semi-empirical model of large-scale magnetospheric electric field, *J. Geophys. Res.*, *78*, 171.
Weimer, D. R. (2001), An improved model of ionospheric electric potentials including substorm perturbations and application to the geospace environment modeling November 24, 1996 event, *J. Geophys. Res.*, *106*, 407.
Young, D. T., H. Balsiger, and J. Geiss (1982), Correlations of magnetospheric ion composition with geomagnetic and solar activity, *J. Geophys. Res.*, *87*, 9077.
Zaharia, S., C. Z. Cheng, and J. R. Johnson (2000), Particle transport and energization associated with substorms, *J. Geophys. Res.*, *105*, 18,741.

N. Y. Ganushkina, Finnish Meteorological Institute, Space Research, FI-00101 Helsinki, Finland. (nataly.ganushkina@fmi.fi)
M. Liemohn, University of Michigan, Space Physics Research Laboratory, Ann Arbor, MI 48109-2143, USA. (liemohn@umich.edu)
A. Milillo, Istituto di Fisica dello Spazio Interplanetario, Via del Fosso del Cavaliere 100, 00133 Roma, Italy. (anna.milillo@ifsi.rm.cnr.it)
T. I. Pulkkinen, Los Alamos National Laboratory, MS D466, Los Alamos, NM 87545, USA. (tuija@lanl.gov)